

Plasmonic external cavity laser refractometric sensor

Meng Zhang,¹ Meng Lu,² Chun Ge,² and Brian T. Cunningham^{2,3,*}

¹Department of Physics, University of Illinois at Urbana–Champaign, Urbana, Illinois 61801, USA

²Department of Electrical and Computer Engineering, University of Illinois at Urbana–Champaign, Urbana, Illinois 61801, USA

³Department of Bioengineering, University of Illinois at Urbana–Champaign, Urbana, Illinois 61801, USA
bcunning@illinois.edu

Abstract: Combining the high sensitivity properties of surface plasmon resonance refractive index sensing with a tunable external cavity laser, we demonstrate a plasmonic external cavity laser (ECL) for high resolution refractometric sensing. The plasmonic ECL utilizes a plasmonic crystal with extraordinary optical transmission (EOT) as the wavelength-selective element, and achieves single mode lasing at the transmission peak of the EOT resonance. The plasmonic ECL refractometric sensor maintains the high sensitivity of a plasmonic crystal sensor, while simultaneously providing a narrow spectral linewidth through lasing emission, resulting in a record high figure of merit for refractometric sensing with an active or passive optical resonator. We demonstrate single-mode and continuous-wave operation of the electrically-pumped laser system, and show the ability to measure refractive index changes with a 3σ detection limit of 1.79×10^{-6} RIU. The demonstrated approach is a promising path towards label-free optical biosensing with enhanced signal-to-noise ratios for challenging applications in small molecule drug discovery and pathogen sensing.

©2014 Optical Society of America

OCIS codes: (140.3600) Lasers, tunable; (250.5403) Plasmonics; (280.4788) Optical sensing and sensors.

References and links

1. E. Stenberg, B. Persson, H. Roos, and C. Urbaniczky, "Quantitative determination of surface concentration of protein with surface plasmon resonance using radiolabeled proteins," *J. Colloid Interface Sci.* **143**(2), 513–526 (1991).
2. S. Löfås, M. Malmqvist, I. Rönnerberg, E. Stenberg, B. Liedberg, and I. Lundström, "Bioanalysis with surface plasmon resonance," *Sens. Actuator B-Chem.* **5**(1–4), 79–84 (1991).
3. J. Homola, "Surface plasmon resonance sensors for detection of chemical and biological species," *Chem. Rev.* **108**(2), 462–493 (2008).
4. A. Artar, A. A. Yanik, and H. Altug, "Fabry–Pérot nanocavities in multilayered plasmonic crystals for enhanced biosensing," *Appl. Phys. Lett.* **95**(5), 051105 (2009).
5. M. E. Stewart, N. H. Mack, V. Malyarchuk, J. A. N. T. Soares, T.-W. Lee, S. K. Gray, R. G. Nuzzo, and J. A. Rogers, "Quantitative multispectral biosensing and 1D imaging using quasi-3D plasmonic crystals," *Proc. Natl. Acad. Sci. U.S.A.* **103**(46), 17143–17148 (2006).
6. V. Malyarchuk, F. Hua, N. Mack, V. Velasquez, J. White, R. Nuzzo, and J. Rogers, "High performance plasmonic crystal sensor formed by soft nanoimprint lithography," *Opt. Express* **13**(15), 5669–5675 (2005).
7. D. Chanda, K. Shigeta, T. Truong, E. Lui, A. Mihi, M. Schulmerich, P. V. Braun, R. Bhargava, and J. A. Rogers, "Coupling of plasmonic and optical cavity modes in quasi-three-dimensional plasmonic crystals," *Nat. Commun.* **2**, 479 (2011).
8. Y. Shen, J. Zhou, T. Liu, Y. Tao, R. Jiang, M. Liu, G. Xiao, J. Zhu, Z.-K. Zhou, X. Wang, C. Jin, and J. Wang, "Plasmonic gold mushroom arrays with refractive index sensing figures of merit approaching the theoretical limit," *Nat. Commun.* **4**, 2381 (2013).
9. T. W. Ebbesen, H. J. Lezec, H. F. Ghaemi, T. Thio, and P. A. Wolff, "Extraordinary optical transmission through sub-wavelength hole arrays," *Nature* **391**(6668), 667–669 (1998).
10. T.-Y. Chang, M. Huang, A. A. Yanik, H.-Y. Tsai, P. Shi, S. Aksu, M. F. Yanik, and H. Altug, "Large-scale plasmonic microarrays for label-free high-throughput screening," *Lab Chip* **11**(21), 3596–3602 (2011).

11. P. Nagpal, N. C. Lindquist, S.-H. Oh, and D. J. Norris, "Ultrasoother patterned metals for plasmonics and metamaterials," *Science* **325**(5940), 594–597 (2009).
12. M. R. Gartia, A. Hsiao, A. Pokhriyal, S. Seo, G. Kulsharova, B. T. Cunningham, T. C. Bond, and G. L. Liu, "Colorimetric plasmon resonance imaging using nano lycurgus cup arrays," *Adv. Opt. Mater.* **1**(1), 68–76 (2013).
13. A. V. Kabashin, P. Evans, S. Pastkovsky, W. Hendren, G. A. Wurtz, R. Atkinson, R. Pollard, V. A. Podolskiy, and A. V. Zayats, "Plasmonic nanorod metamaterials for biosensing," *Nat. Mater.* **8**(11), 867–871 (2009).
14. B. Cunningham, B. Lin, J. Qiu, P. Li, J. Pepper, and B. Hugh, "A plastic colorimetric resonant optical biosensor for multiparallel detection of label-free biochemical interactions," *Sens. Actuator B-Chem.* **85**(3), 219–226 (2002).
15. I. M. White, H. Oveys, and X. Fan, "Liquid-core optical ring-resonator sensors," *Opt. Lett.* **31**(9), 1319–1321 (2006).
16. S. Arnold, M. Khoshshima, I. Teraoka, S. Holler, and F. Vollmer, "Shift of whispering-gallery modes in microspheres by protein adsorption," *Opt. Lett.* **28**(4), 272–274 (2003).
17. H. Yi, D. S. Citrin, and Z. Zhou, "Highly sensitive silicon microring sensor with sharp asymmetrical resonance," *Opt. Express* **18**(3), 2967–2972 (2010).
18. C. Ge, M. Lu, S. George, T. A. Flood, Jr., C. Wagner, J. Zheng, A. Pokhriyal, J. G. Eden, P. J. Hergenrother, and B. T. Cunningham, "External cavity laser biosensor," *Lab Chip* **13**(7), 1247–1256 (2013).
19. M. Lu, S. S. Choi, U. Irfan, and B. T. Cunningham, "Plastic distributed feedback laser biosensor," *Appl. Phys. Lett.* **93**(11), 111113 (2008).
20. S. Kita, K. Nozaki, and T. Baba, "Refractive index sensing utilizing a cw photonic crystal nanolaser and its array configuration," *Opt. Express* **16**(11), 8174–8180 (2008).
21. L. He, S. K. Ozdemir, J. Zhu, W. Kim, and L. Yang, "Detecting single viruses and nanoparticles using whispering gallery microlasers," *Nat. Nanotechnol.* **6**(7), 428–432 (2011).
22. D. Wang, X. Yu, and Q. Yu, "Tuning multiple Fano and plasmon resonances in rectangle grid quasi-3D plasmonic-photonic nanostructures," *Appl. Phys. Lett.* **103**(5), 053117 (2013).
23. S.-H. Chang, S. Gray, and G. Schatz, "Surface plasmon generation and light transmission by isolated nanoholes and arrays of nanoholes in thin metal films," *Opt. Express* **13**(8), 3150–3165 (2005).
24. Y. Tan, A. Chu, M. Lu, and B. T. Cunningham, "Distributed feedback laser biosensor noise reduction," *IEEE Sens. J.* **13**(5), 1972–1978 (2013).
25. A. A. Yanik, A. E. Cetin, M. Huang, A. Artar, S. H. Mousavi, A. Khanikaev, J. H. Connor, G. Shvets, and H. Altug, "Seeing protein monolayers with naked eye through plasmonic Fano resonances," *Proc. Natl. Acad. Sci. U.S.A.* **108**(29), 11784–11789 (2011).
26. M. Zhang, C. Ge, M. Lu, Z. Zhang, and B. T. Cunningham, "A self-referencing biosensor based upon a dual-mode external cavity laser," *Appl. Phys. Lett.* **102**(21), 213701 (2013).
27. M. Zhang, J. Peh, P. J. Hergenrother, and B. T. Cunningham, "Detection of protein-small molecule binding using a self-referencing external cavity laser biosensor," *J. Am. Chem. Soc.* **136**(16), 5840–5843 (2014).
28. I. D. Block, N. Ganesh, L. Meng, and B. T. Cunningham, "A sensitivity model for predicting photonic crystal biosensor performance," *IEEE Sens. J.* **8**(3), 274–280 (2008).
29. A. Cattoni, P. Ghenuche, A.-M. Haghiri-Gosnet, D. Decanini, J. Chen, J.-L. Pelouard, and S. Collin, " $\lambda/1000$ plasmonic nanocavities for biosensing fabricated by soft UV nanoimprint lithography," *Nano Lett.* **11**(9), 3557–3563 (2011).
30. S. Y. Lee, S.-H. Kim, S. G. Jang, C.-J. Heo, J. W. Shim, and S.-M. Yang, "High-fidelity optofluidic on-chip sensors using well-defined gold nanowell crystals," *Anal. Chem.* **83**(23), 9174–9180 (2011).
31. S. H. Lee, T. W. Johnson, N. C. Lindquist, H. Im, D. J. Norris, and S.-H. Oh, "Linewidth-optimized extraordinary optical transmission in water with template-stripped metallic nanohole arrays," *Adv. Funct. Mater.* **22**(21), 4439–4446 (2012).

1. Introduction

Surface plasmon resonance (SPR) biosensors that measure changes in surface-adsorbed refractive index as biomolecules adsorb onto metal surfaces have been used effectively to analyze biomolecular interactions since the first demonstration in 1991 [1, 2]. Due to strong light-matter interaction provided by enhanced near-fields adjacent to a metal/dielectric interface, SPR biosensors demonstrate label-free molecule detection with excellent sensitivity [3], leading to a variety of applications in life science research, pharmaceutical discovery, and medical diagnostics. Building upon the commercial success of SPR biosensors utilizing the Kretschmann configuration, recent work on SPR sensing based on periodically nanostructured metal films has generated intense interest [4–8]. The extraordinary optical transmission (EOT) effect [9], arising from plasmon interactions between periodic arrays of metallic elements, leads to large field enhancement and high sensitivity to surface-localized refractive index changes. In contrast to the Kretschmann configuration, plasmonic crystal

structures do not require physical contact to a coupling prism, enabling detection via measurement of the reflection or transmission spectra.

Extensive effort has been devoted to further enhancing the performance of plasmonic nanostructured sensors for the most challenging biosensing applications, where plasmonic devices with both narrow resonant linewidth and high refractive index sensitivity are required to detect extremely small resonance shifts. Fabrication methods for plasmonic nanostructures have been developed to precisely control their nanometer-scale features [10] and to reduce surface roughness [11], leading to reduced scattering losses and resonant linewidth (Γ , as measured by full width at half maximum of the resonant transmission spectrum). Novel designs for plasmonic nanostructures that redistribute the plasmon-enhanced electric fields have been demonstrated with the goal of making the resonant field accessible to the surrounding environment [12, 13], so as to achieve greater sensitivity (S_b , as measured by the bulk refractive index sensitivity $S_b = \Delta\lambda/\Delta n$, where $\Delta\lambda$ is the shift in resonant wavelength induced by a change in refractive index of liquid on the sensor surface of Δn). However, due to ohmic losses of metal, inherent to all *passive* SPR sensing approaches, the advantage of high sensitivity of SPR sensing is offset by the moderate resolution for sensing small wavelength shifts due to the broad resonance. As a result, several types of high- Q dielectric resonators achieve detection figure of merit (FOM) metrics that far exceed that of SPR, where the FOM is defined as $\text{FOM} = S_b/\Gamma$, in order to simultaneously capture the effects of the magnitude of the refractive index induced resonant shift and the ability to measure small wavelength shifts. Alternative passive optical resonator approaches that report FOM values greater than SPR include photonic crystals [14], liquid-core optical fibers [15], whispering-gallery mode microspheres [16], and microring resonators [17]. Because increased Q for an optical resonator has generally also resulted in reduced S_b [18], there has been a great deal of research focused on development of *active* optical resonators that achieve narrow resonant linewidth without sacrificing sensitivity through the process of stimulated emission [18–21].

In this paper, we experimentally demonstrate a plasmonic external cavity laser (ECL) refractometric sensor, which achieves sharp resonant linewidth associated with external cavity laser emission, while at the same time maintaining the high S_b associated with SPR. In our approach, a plasmonic crystal sensor with high quality factor EOT resonance is utilized as the wavelength-selective element in an ECL cavity. Through the incorporation of broadband optical gain, single-mode lasing at the peak transmission wavelength of the plasmonic crystal is achieved. Variations of refractive index on the plasmonic sensor surface lead to a shift of the transmission peak of the EOT resonance, which subsequently tunes the lasing wavelength of the plasmonic ECL with the same magnitude. The plasmonic ECL performs refractometric measurements by generating lasing wavelength shifts that are easily detected with a laser spectrum analyzer. We demonstrate electrically-pumped, continuous-wave refractive-index tuning of single-wavelength lasing with the plasmonic ECL. Since the lasing emission, mediated by the stimulated emission process, has a significantly narrower linewidth than that of the EOT resonance, the plasmonic ECL improves the spectral resolution of the plasmonic crystal sensor without sacrificing its high sensitivity, resulting in an overall FOM that is superior to any previously reported approach. The fundamental approach reported here can form the basis of a new generation of plasmonic biosensors for label-free biosensing.

2. Methods

2.1 Design and fabrication of plasmonic crystal

The plasmonic crystal, comprised of a periodically nanostructured metal film, was fabricated with a plastic-based nanoreplica molding process on a mechanically flexible substrate [14]. An imprinted epoxy replica of a two-dimensional nanopatterned silicon stamp served as the template for production of the plasmonic lattice. The epoxy substrate had a square array of cylindrical wells with a lattice period of 500 nm, hole diameter of 210 nm and post depth of

150 nm. Uniform e-beam evaporation of a 40-nm-thick gold film coated the epoxy surface as well as the bottom of the cylindrical wells, creating a quasi-3D plasmonic crystal. The plasmonic crystal therefore consists of a layer of thin gold film with a nanohole array and an underlying gold nanodisk array (Fig. 1(a)). Figure 1(b) shows an optical image of the sensor surface with a size of 8 mm × 8 mm as defined by the effective area of the silicon stamp. Figures 1(c) and 1(d) present top- and side-views of scanning electron microscope images of the fabricated plasmonic crystal. The top metal thin film and the bottom metal nanodisks are physically separated, with no observable gold coating on the sidewalls. The design of the plasmonic crystal maximizes the strength of plasmon resonance in the desired spectral range. The plasmonic resonances of the periodically nanostructured top metal layer and the bottom gold nanodisks spectrally overlap (Figs. 5 and 6). The presence of these two resonances results in a significant reduction in the spectral linewidth of the quasi-3D plasmonic crystal (Fig. 7), making the device an effective narrowband transmission filter in the near infrared (NIR) part of the optical spectrum.

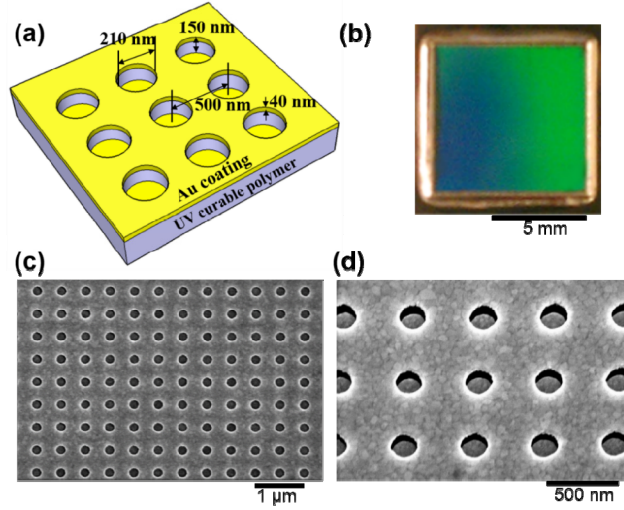


Fig. 1. (a) Schematic illustration of the plasmonic crystal. (b) Optical image of the fabricated plasmonic crystal with a size of 8 mm × 8 mm. (c) and (d) Top- and side-view of scanning electron microscope images of the fabricated plasmonic crystal surfaces.

2.2 Resonance modes of plasmonic crystal

We performed polarization-resolved angle-dependent study of the zero-order transmission characteristics of the fabricated device. The device was mounted in a transmission fixture, in which it was illuminated with collimated, linearly polarized white light. The spectral wavelengths and transmission efficiencies of plasmon resonances for *p*-polarized illumination as a function of the launch angle, θ , along the Γ -X axis are mapped in the dispersion diagram, as illustrated in Figs. 2(a) and 2(b). The calculated dispersion of the SPP-Bloch wave (BW) modes is also presented in Figs. 2(a) and 2(b), where the resonant condition is described by the Bragg coupling equation:

$$|\mathbf{k}_{\parallel} + i\mathbf{G}_x + i\mathbf{G}_y| = \frac{\omega}{c} \sqrt{\frac{\epsilon_d \epsilon_m}{\epsilon_d + \epsilon_m}} \quad (1)$$

where \mathbf{k}_{\parallel} is the in-plane wave vector, *i* and *j* specify the order of the SPP-BW modes, \mathbf{G}_x and \mathbf{G}_y are reciprocal vectors which are inversely proportional to the lattice constant, ω

and c are the momentum and speed of free-space light, ϵ_d and ϵ_m are the electric permittivity of the adjacent dielectric and the metal.

Along the Γ -X axis, a distinct transmission mode, which manifests itself as the strongest and narrowest plasmon resonance, shifts to longer wavelength as the launch angle is increased. The overall trends of this mode are in good agreement with the simple dispersion relation predicted by Eq. (1), indicating that the resonance originates from the $(-1, 0)$ SPP-BW mode along the gold/air interface. Since the plasmonic crystal investigated in this study is designed to operate as a label-free biosensor in aqueous media, the dispersion of the device when immersed in water was also characterized. The refractive index change of the cover media from air to water resulted in a large red shift of the plasmon resonance modes. The distinct EOT mode associated with $(-1, 0)$ SPP resonance along the gold/water interface was also observed as the strongest and narrowest plasmon resonance, as shown in Fig. 2(b). The narrow linewidth, combined with the strong transmission intensity of this resonant mode enables the device to perform as a transmission filter to select the lasing wavelength in a laser cavity. In addition, the transmission filter based on this resonance mode is tunable over a wide wavelength range, as the resonance peak can be modulated by changing the launch angle.

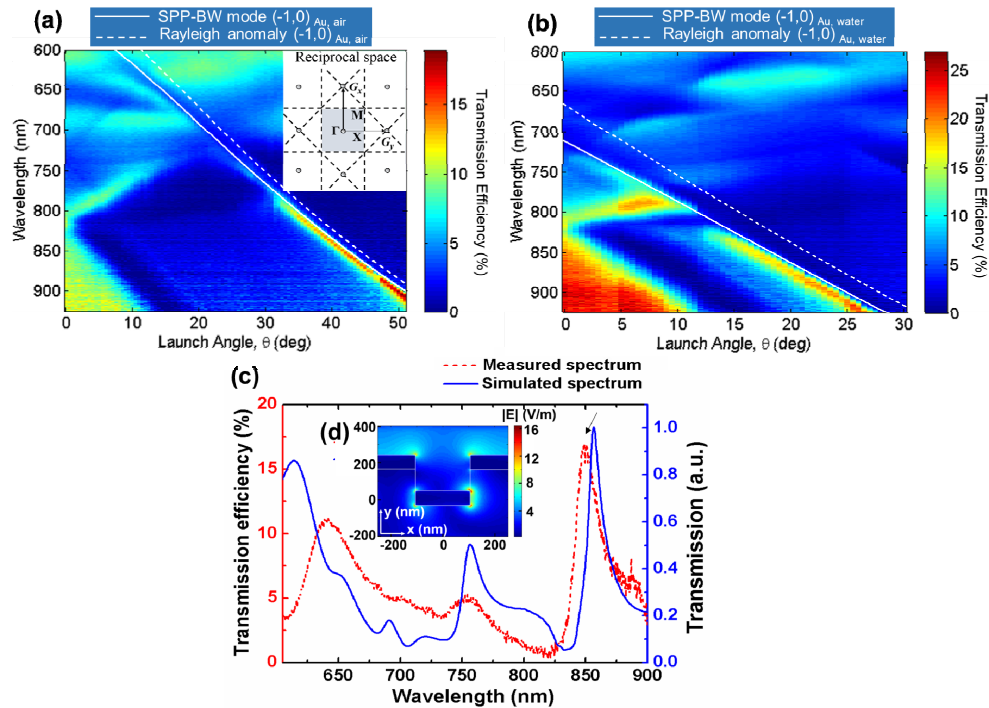


Fig. 2. Experimental transmission spectra as a function of incident angle θ for white, p -polarized illumination along the Γ -X direction of the plasmonic crystal (a) with air as the background media and launch angle varied from $\theta = 0^\circ$ to 50° and (b) with water as the background media and launch angle varied from $\theta = 0^\circ$ to 30° . Calculated dispersion curves of SPP-BW mode (solid lines) and Rayleigh anomaly (dashed lines) are superimposed. Inset: Schemes of the square lattice structure in reciprocal space. (c) Measured (red dashed curve) and simulated (blue solid curve) transmission spectra for the plasmonic crystal with launch angle $\theta = 16^\circ$. Inset (d) Simulated electric field intensity distribution for the peak at $\lambda = 850$ nm.

Full three-dimensional finite-difference time-domain simulations with appropriate boundary conditions were used to calculate the transmission spectra and the electromagnetic

field distributions in and around the metal nanostructures of the device. With a launch angle of 16° , experimental and simulated transmission spectra of the plasmonic crystal in water are shown together in Fig. 2(c). The calculated near field intensity patterns at the peak transmission wavelength, as shown in Fig. 2(d), confirm that the resonance is associated with the excitation of a SPP-BW mode near the gold/water interface of the top nanohole array. Additionally, the near-field distribution suggests the excitation of the localized SPR modes of the bottom nanodisks. The simultaneous presence of plasmon resonances of the nanohole array and nanodisk array creates complex responses that enables strong linewidth narrowing for the observed EOT phenomenon [4, 5, 22, 23]. Besides the high quality-factor plasmonic resonances, the enhanced near-fields associated with the resonance penetrate evanescently into the surrounding media from the gold/water interface. Strong concentration of the electromagnetic field in the dielectric medium allows strong light-matter interactions, suggesting the high sensitivity for refractive index sensing.

2.3 Plasmonic external cavity laser design

The plasmonic ECL detection instrument is comprised of a semiconductor optical amplifier (SOA), two polarization maintaining (PM) single-mode optical fibers, two NIR mirrors and the plasmonic crystal, as shown in the schematic diagram in Fig. 3(a). The SOA (SOA-371, Superlum Inc., peak wavelength $\lambda = 850$ nm, and spectral width $\Delta\lambda = 40$ nm) has both edge facets coated with an anti-reflection layer, and is coupled to a single-mode PM fiber with a length of 1 m. The output from the fiber on each side, through a collimating lens, is normally reflected against a NIR mirror to form an optical cavity. The plasmonic crystal is mounted on a rotation stage with an adjustable angle, and is inserted into the Fabry-Perot cavity to selectively transmit the narrow range of resonant wavelengths. The transmitted light is efficiently coupled back into the SOA, where it is amplified. Due to the broadband nature of the SOA and NIR mirrors, the peak transmission wavelength of the plasmonic crystal first achieves the threshold condition for lasing, in which the resonant wavelength of the plasmonic crystal determines the single-mode lasing wavelength of the ECL cavity. A detection instrument such as a spectrometer or a laser spectrum analyzer may be utilized to quantify the lasing wavelength, and to dynamically monitor lasing wavelength shifts.

As the plasmonic ECL biosensor resonates, a high intensity electromagnetic wave is established on the plasmonic crystal/media interface (Fig. 2(d)). Changes of the bulk refractive index or the attachment of biomolecules will shift the resonant transmission wavelength, and subsequently lead to a lasing wavelength shift in the ECL system. The use of a two meter long optical fiber cavity provides mode spacing of 0.08 pm [18], ensuring detection of small wavelength shifts without hopping between modes in a discontinuous manner. While the plasmonic crystal is a passive resonator with moderate quality factor ($Q \sim 100$), the active laser resonator achieves extremely narrow linewidth through the process of stimulated emission and offers substantially greater spectral resolution. At the same time, the capability of the plasmonic crystal to register changes of refractive index with high sensitivity is maintained.

3. Results

3.1 Characterization of the plasmonic external cavity laser

The relationship between the laser output power and the injection current is shown in Fig. 3(b), demonstrating a threshold current of 55 mA. The transmission spectra of the plasmonic crystal and the laser emission spectra of the ECL are plotted together in Figs. 3(c) and 3(d). With a launch angle of $\theta = 42^\circ$ in air, the plasmonic crystal exhibits a resonance at $\lambda = 860$ nm, resulting in lasing emission at $\lambda = 860$ nm (Fig. 3(c)). Similarly, with a launch angle of $\theta = 18^\circ$ in water, lasing at the peak transmission wavelength of $\lambda = 862$ nm is demonstrated (Fig. 3(d)). Using a laser spectrum analyzer (721 A series, Bristol Instruments, Inc. absolute

accuracy ± 0.2 ppm) to measure the ECL emission spectrum, we obtain the full width at half maxima $\Gamma = 21.52$ pm (or Γ (eV) = 3.62×10^{-5} eV). The intense and narrow linewidth emission of the ECL allows the system to resolve extremely small wavelength shifts when used as a refractive index sensor.

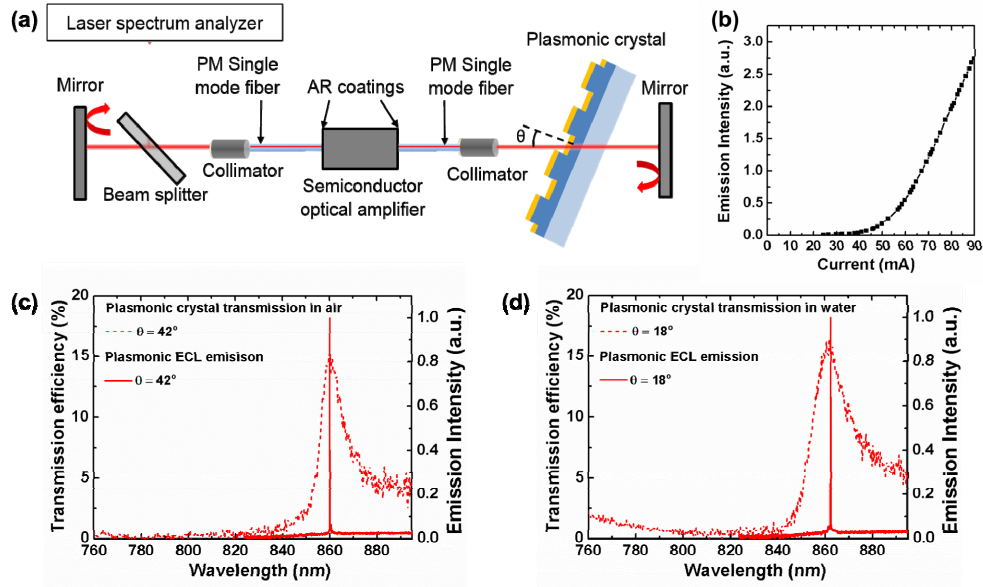


Fig. 3. (a) Schematic drawing of the plasmonic external cavity laser detection instrument. (b) The light v.s. current (L.I.) curve associated with the plasmonic external cavity laser. Overlaid plasmonic crystal transmission spectra and plasmonic ECL laser emission spectra (c) with launch angle $\theta = 42^\circ$ in air and (d) with launch angle $\theta = 18^\circ$ in water.

3.2 Refractive index sensing

To examine the performance of the plasmonic ECL system as a refractive index sensor, we measured the lasing spectra with the plasmonic crystal immersed in liquid samples of different mixtures of dimethyl sulfoxide (DMSO) and deionized (DI) water. The launch angle was set at 17° , and this specific angle was chosen so that the resonant transmission intensity of the plasmonic crystal is maximized near the peak gain region of the SOA. The concentrations of the DMSO solution in water ranged from 0% to 8%. As we increased the refractive index of liquid on the plasmonic crystal surface, the resonances of the plasmonic crystal shifted to longer wavelengths, which subsequently modulates the lasing wavelength value (LWV) of the plasmonic ECL. The normalized lasing spectra are plotted together in Fig. 4(a). The linear bulk refractive index sensitivity was measured to be $S_b = 547$ nm/RIU over a dynamic range of 7 nm (Fig. 4(b)). In addition, bulk refractive index tuning of the system demonstrates that single-mode lasing is achieved over a wide range of wavelengths. The full operating range of the system is determined by the gain spectrum of the SOA, which has been selected to provide gain between $\lambda = 830$ -870 nm.

To determine spectral resolution and to identify the sensing limitations of the plasmonic ECL, we measured the time-sequence LWVs as we introduced a small refractive index variation to the plasmonic crystal. The LWVs were rapidly determined using the aforementioned laser spectrum analyzer, which utilizes a scanning-mirror Michelson interferometer and does not require a separate spectral fitting algorithm to identify the peak position, greatly simplifying the data analysis process. A stable LWV baseline was established when the plasmonic crystal was immersed in DI water. Next, we introduced 0.05% DMSO solution through a flow cell that was attached to the sensor surface. The

solutions were introduced to the plasmonic crystal through a flow cell, within which the plasmonic crystal was incorporated as the bottom surface. The flow chamber has a height of 3 mm, width of 9 mm, and length of 18 mm, and was fabricated by cutting Poly(methyl methacrylate) (PMMA) into the desired dimensions. Two cylindrical openings at the ends of the flow cell were tapped and screwed in with 1/16" hose barb adapter connected to tubing as inlet and outlet. The solutions were introduced through the flow cell using a syringe. We measured the time-sequence LWV after signal stabilization, and observed a LWV shift of 23.60 pm, as shown in Fig. 4(b) inset. Since there was no fluid mixing process during this refractometric measurement, the LWV shift was caused by abruptly changing the liquid from DI water to DMSO solution homogeneously in the flow cell. The sensor output noise was quantitatively characterized with the standard deviation $\sigma = 0.62$ pm. The limit of detection (LOD) $= 3\sigma / S_b = 3.38 \times 10^{-6}$ RIU is obtained. With a commonly used "boxcar" technique to average 10 adjacent LWV measurements to reduce noise [24], the LOD is easily further reduced to 1.79×10^{-6} RIU. Note that this value is obtained without any form of thermal control or referencing, and that it represents the ability to differentiate refractive index differences with 3σ resolution (many publications utilize 1σ values).

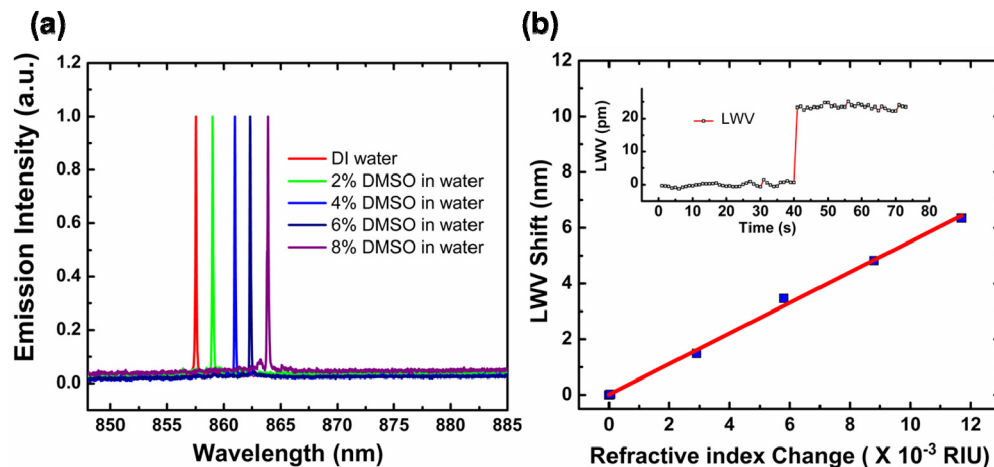


Fig. 4. (a) Measured lasing spectra of the plasmonic ECL with the plasmonic crystal immersed in DMSO-water mixture solutions with varying compositions at the fixed launch angle of $\theta = 17^\circ$. (b) Bulk sensitivity characterization. Laser emission wavelength shifts as the sensor was exposed to liquid media with different refractive index. A linear fit to the experimentally obtained data reveals a bulk sensitivity of 547 nm/RIU. Inset: Measured response during a refractometric experiment for the plasmonic ECL. The refractive index change was 7.5×10^{-5} via the addition of DMSO.

4. Discussion

As described briefly in the Introduction, a widely adopted metric for comparison between resonant optical biosensors is the FOM. For the plasmonic ECL, a value of $FOM = 2.60 \times 10^4$ is obtained. As listed in Table 1, this value is nearly two orders of magnitude larger than the previously reported record high FOMs obtained with a periodically nanostructured plasmonic sensor [8, 25]. This extraordinary FOM results from the unique combination of the narrow linewidth of stimulated emission and the high refractive index sensitivity of SPR. Importantly, this method of forming a resonant cavity where the plasmonic sensors interact with optical gain to achieve narrow resonant linewidth is not limited to the plasmonic crystal structure introduced in this paper, but is widely applicable to other plasmonic sensors based on EOT resonances.

Recently, several laser-based label-free biosensors, such as the distributed feedback laser [19], the photonic crystal laser [20], and the whispering gallery microlaser [21], have been

reported to achieve high spectral resolution by generating a high intensity and narrow linewidth output through the stimulated emission process. Although exciting capabilities have been demonstrated, as listed in Table 2, many of these devices require a large optical pumping source and are only capable of operating in pulsed mode. Additionally, degradation of dye, as a result of photo-damage during pulsed measurements, leads to decreased lasing stability and reduced sensor performance. Compared to these devices, the utilization of an external laser cavity to physically separate the optical gain from the sensor surface represents a fundamentally different approach [18, 26, 27]. This arrangement results in a robust high spectral resolution detection system that utilizes an electrical pump source, operates in CW mode, while using a sensor structure that can be fabricated inexpensively over large surface areas. Because SPR sensors deliver greater refractive index sensitivity than dielectric optical resonators, the ability of plasmonic ECL to overcome the low- Q limitation of SPR through a stimulated emission system results in the potential for improved sensor performance compared to previous demonstrated laser biosensors.

In conclusion, we developed a high resolution refractometric sensor based upon a plasmonic ECL that combines the high sensitivity of SPR refractive index sensing with a tunable ECL. To achieve this, we fabricated a polymer-based replica-molded quasi-3D plasmonic crystal sensor, which generates a high quality factor EOT resonance from strong plasmon coupling of the top nanohole array and the bottom nanodisk array. We utilized this spectrally sharp plasmon resonance mode to select and to tune lasing wavelength in the ECL, resulting in lasing at the peak transmission wavelength. We have demonstrated single-mode operation of the plasmonic ECL system with a large refractive-index tuning range of 7 nm. The ability to measure refractive index changes with a detection limit of 1.79×10^{-6} RIU is demonstrated. As a result of the unique combination of refractive index sensitivity of SPR and narrow linewidth of laser emission, a record high experimental FOM was obtained. With the integration of microfluidic channels and bioaffinity assays, the plasmonic external cavity laser system offers the potential for a novel label-free biosensing approach towards challenging applications, such as detection of small molecule interactions with immobilized proteins, detection of low-abundance proteins in a specimen. Based on the estimated surface mass density sensitivity [28] and the measured spectral resolution, a mass density resolution of 2×10^{-19} g/ μm^2 is predicted for biosensing applications with the plasmonic external cavity laser system. As the technology evolves, we expect to be able to probe small areas with the SOA on the plasmonic crystal surface with an area as low as $1 \times 1 \mu\text{m}^2$. As a single antibody molecule has a mass of $\sim 2.5 \times 10^{-19}$ g, we believe that single antibody molecule detection resolution will become possible with this technology.

Appendix A

To better understand the origins of the resonance modes of the quasi-3D plasmonic crystal (Fig. 2), we performed FDTD simulations to model the transmission spectra and the electromagnetic field distributions for three types of plasmonic structures: the bottom gold nanodisk array only, the top gold film with nanohole array only, and the quasi-3D plasmonic crystal structure.

The transmission spectrum of the bottom gold nanodisk array when immersed in water reveals a resonant mode at 870 nm (Fig. 5(a)) with launch angle $\theta = 16^\circ$. The electric field associated with this resonance is concentrated at the edges of the gold disk (Fig. 5(b)), indicating the excitation of LSPR of the gold nanodisk. The transmission spectrum of the top gold nanohole film, as shown in Fig. 6(a), exhibits a peak at 865 nm, associated with intense near-field intensity along the gold/water interface (Fig. 6(b)). This transmission peak arises from the $(-1,0)$ SPP-BW mode and Rayleigh anomaly on the gold/water side of the device predicted by Eq. (1). This mode red-shifts as the incident angle increases. In our case, with 16° incident angle, the SPP-BW mode of the nanohole array spectrally overlaps with the

LSPR of the gold nanodisk. Thus, concurrence of plasmonic resonances of both the nanodisk array and the nanohole array is expected in the quasi-3D plasmonic crystal.

We performed simulations for the quasi-3D plasmonic crystal, and indeed observed a strong peak at 860 nm (Fig. 7(a)) which has nearly the same spectral position as the resonant peaks of both the bottom nanodisk array and the top gold nanohole film. This suggests the simultaneous excitation of both the LSPR of the gold nanodisk and the SPP-BW mode of the nanohole array, and is further confirmed by the near-field distributions shown in Fig. 7(b). Light transmits through the plasmonic crystal *via* coupling between these two resonant modes, achieving extraordinary light transmission with high quality factor.

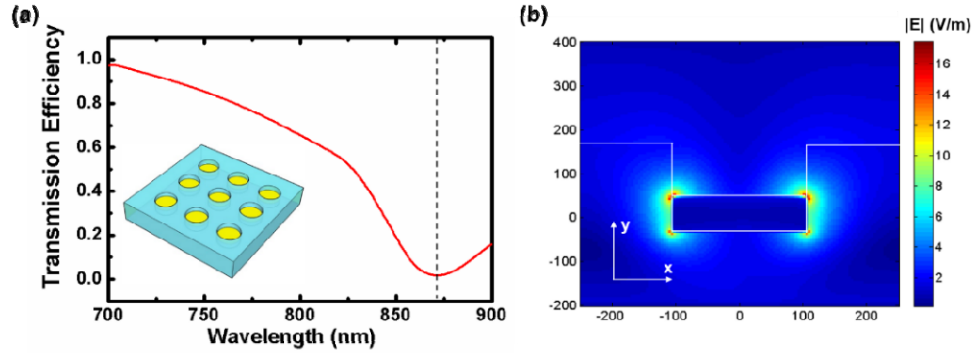


Fig. 5. (a) Simulated transmission spectrum for the structure composed of only the bottom nanodisk array. (b) Simulated electric field intensity distributions for the resonance transmission dip.

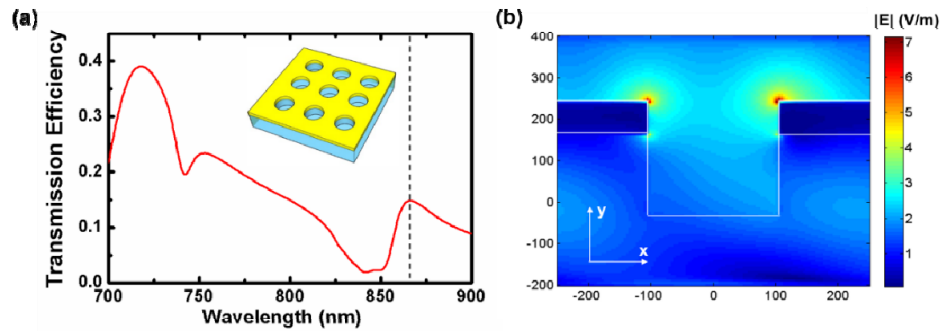


Fig. 6. (a) Simulated transmission spectrum for the structure composed of only the top metal film with nanohole array. (b) Simulated electric field intensity distributions for the resonance transmission peak.

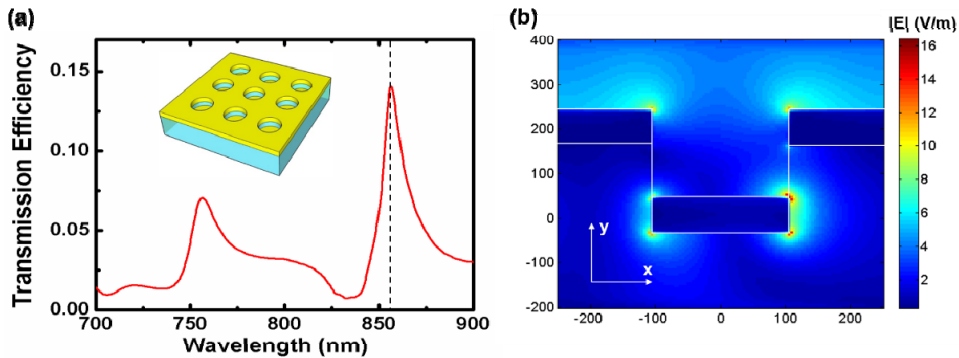


Fig. 7. (a) Simulated transmission spectrum for the quasi 3D plasmonic crystal composed of top nanohole array and bottom nanodisk array. (b) Simulated electric field intensity distributions for the resonance transmission peak.

Appendix B

Table 1. Summary of the Refractive Index Sensitivities and FOM Values of Plasmonic Biosensors/Refractometric Sensors

Nanostructures	λ	FWHM		Sensitivity		FOM	FOME
	nm	nm	eV	nm/RIU	eV/RIU		
Plasmonic crystal ECL	850	0.021	3.6×10^{-5}	547	0.94	2.60×10^4	2.59×10^4
Plasmonic gold mushroom arrays [8]	1288	9.5	7.1×10^{-3}	1015	0.75	106.8	105.6
Plasmonic nanohole devices [25]	820	4.42	8.3×10^{-3}	717		162.2	144.3
Microcavity arrays [29]	900	19		405		21.3	
Gold nanowell crystal [30]	750		0.248	570	1.024		4.1
Template-stripped metallic nanohole arrays [31]	700	9.5		494		52	
Plasmonic nanorod metamaterials [13]	1230	96.9		32,000		330	

Table 2. Summary of the Refractive Index Sensitivity and Lasing Mechanism for Various Laser Biosensors

Laser system	λ (nm)	Sb (nm/RIU)	Pump method, Operating mode	Gain material, External/integrated gain
Plasmonic external cavity laser	850	549	Electrical injection, CW	SOA, external gain
External cavity laser [18]	850	212	Electrical injection, CW	SOA, external gain
Distributed feedback laser [19]	588	100	Optical pumped, pulsed	Laser dye, integrated gain
Photonic crystal laser [20]	1600	350	Optical pumped, CW	SQW/MQW, integrated gain
Whispering gallery microlaser [21]	1550	-	Optical pumped, CW	Er ⁺ ions, integrated gain

Acknowledgments

The authors gratefully acknowledge the National Science Foundation (CBET 1132225) and National Institutes of Health (R21EB009695 and R01GM90220) for providing financial support for this work.